



# Influence of Machine Stiffness on the Portevin–Le Chatelier Effect of Ti-12Mo Alloy Based on a Modified McCormick Constitutive Model

Shiyuan Luo<sup>1,2</sup> · Liang Xiao<sup>1,2</sup> · Jun Jiang<sup>1,2</sup> · Jia Li<sup>1,3</sup> · Liangcai Zeng<sup>1,3</sup>

Received: 21 November 2023 / Accepted: 7 March 2024

© The Author(s) under exclusive licence to The Korean Institute of Metals and Materials 2024

## Abstract

An improved 3D FE model, considering machine stiffness effect and strain dependent parameters in an embedded modified McCormick's constitutive model, is developed to numerically investigate the spatiotemporal characteristics of the PLC effect in Ti-12Mo alloy tensile tests. The material parameters of the modified McCormick's model are calibrated in details, and the simulated results are compared with experiment and literature ones. Then, the influence of machine stiffness on the spatiotemporal behaviors of the PLC effect in Ti-12Mo alloy are quantitatively analyzed. The results show that the improved FE model has a higher simulation accuracy in term of stress drop frequency. Moreover, the average stress drop magnitude decreases and the number of stress drops increases with the increase of machine stiffness, which are mainly owing to the decrease of aging time. Furthermore, the PLC band width decreases as increasing machine stiffness, which is attributed to the decrease of driving force for band nucleation. Besides, the continuous and hopping propagations of the PLC band are observed, and the propagation continuity obviously increases as increasing machine stiffness, which is mainly related to the increase of spatial coupling force.

**Keywords** Ti-12Mo alloy · Portevin–Le Chatelier effect · Machine stiffness · FE modeling

## 1 Introduction

Ti-xMo alloys have high specific strength, strong corrosion resistance and great biocompatibility, which can be widely used in many fields ranging from aeronautics to biomedical devices [1–3]. However, Portevin–Le Chatelier (PLC) effect, as a type of plastic instability, is found in these alloys, which results in the serious decreases of material elongation, impact toughness and fatigue life [4–6]. Hence, for improving mechanical properties, reliability and service life, it is of great importance to accurately

predict the spatiotemporal characteristics of the PLC effect in Ti-xMo alloys.

Until now, a large amount of work has been performed on simulating the PLC effect in various alloys and the corresponding constitutive models were put forward. Hereinto, based on the interactions of different dislocations, Ananthakrishna [7] developed a nonlinear mathematical model, namely AK model, to predict the temporal behaviors of the PLC effect. Sarmah et al. [8] employed the AK model to analyze the correlation between the stress drop magnitude and the propagation property of the PLC band. Then, Kubin and Estrin [9] established a mathematical model, called KE model, which provides a link between the microscopic and macroscopic aspects of nonuniform deformation associated with the PLC effect. Moreover, Kok et al. [10] utilized the KE model to observe the propagation type of the PLC band in Al–Mg alloy tensile procedure. However, it should be pointed out that the above models have difficulties in quantitatively describing the spatiotemporal characteristics of the PLC effect. Therefore, McCormick [11] proposed a constitutive model, known as MC model, which takes into account the time dependence of the solute composition at mobile dislocations. Thereafter, Zhang et al. [12] embedded the MC

✉ Shiyuan Luo  
shiyuanluo@wust.edu.cn

<sup>1</sup> Key Laboratory of Metallurgical Equipment and Control Technology, Ministry of Education, Wuhan University of Science and Technology, Wuhan 430081, China

<sup>2</sup> Hubei Key Laboratory of Mechanical Transmission and Manufacturing Engineering, Wuhan University of Science and Technology, Wuhan 430081, China

<sup>3</sup> Precision Manufacturing Institute, Wuhan University of Science and Technology, Wuhan 430081, China

model into ABAQUS software to simulate the spatiotemporal behaviors of the PLC effect in Al–Mg–Si alloy tensile tests. Graff et al. [13] employed the MC model to investigate the influences of notched angles and crack lengths on the spatiotemporal characteristics of the PLC effect in aluminum alloy tensile tests. Benallal et al. [14] implemented the MC model into the LS-DYNA software to simulate the morphology and velocity variations of the PLC band during an AA5083 aluminum alloy tensile process. Furthermore, through embedding the MC constitutive equations into ABAQUS/Standard software by UMAT subroutine, Böhlke et al. [15] studied the effect of applied strain rate on the critical strain of the PLC effect in 2024 aluminum alloy tensile tests. Subsequently, Mazière et al. [16] also used the MC model to predict the influence of ceramic particle volume fraction on the stress drop magnitude of the PLC effect in an AlCu/Al<sub>2</sub>O<sub>3</sub> composite tensile procedure. In addition, Xue et al. [17] employed the MC model to reproduce the serration morphologies and spatiotemporal patterns of the PLC effect in an AA5182 alloy, and found that the PLC band nucleation is mainly influenced by strain accumulation and strain aging processes. Note that, although a large majority of studies have been devoted to predicting the spatial [18–20] and temporal [21–23] aspects of the PLC effect in various alloys, however, for Ti-xMo alloys, only Luo et al. [24] developed a FE model to simulate the spatiotemporal behaviors of the PLC effect in Ti-12Mo alloy tensile tests, which has a significant limitation in accurately predicting the stress drop frequency and ignores the influence of machine stiffness on the spatiotemporal behaviors of the PLC effect.

Therefore, this paper is aimed to develop an improved 3D FE model embedded with a modified MC constitutive model to investigate the influence of machine stiffness on the spatiotemporal behaviors of the PLC effect in Ti-12Mo alloy tensile tests. For this purpose, a modified MC model is established and its material parameters are identified in details. Then, considering machine stiffness, the improved 3D FE model embedded with the modified MC model is established by using ABAQUS 6.14 software and verified by experiments. Finally, a comparison with previous simulation work is carried out and the influence of machine stiffness on the spatiotemporal behaviors of the PLC effect in Ti-12Mo alloy tensile tests are qualitatively analyzed.

## 2 Material Preparation and Tensile Testing

### 2.1 Material Preparation

Ti-12Mo (wt%) alloy is synthesized with pure titanium (99.95 wt%) and molybdenum (99.99 wt%) by using

semi-levitation melting furnace (Fig. 1a). Then, to ensure the homogeneous distribution of compositions, a heat treatment at 950 °C for 20 h followed by quenching in water is performed for above ingots (Fig. 1b). Moreover, after removing the surface oxide layers of the ingots with an acidic bath (50 HF + 50 HNO<sub>3</sub> (Vol%)), they are cold rolled into sheets with the final thickness of about 1 mm. Subsequently, tensile specimens with a gauge size of 15 × 3 × 1 mm<sup>3</sup> are cut from the rolled sheets along the rolling direction, as shown in Fig. 1c. Finally, a recrystallization treatment at 870 °C for 0.5 h is performed for these specimens.

### 2.2 Tensile Testing

Ti-12Mo alloy tensile tests are conducted on Gleeble 3500 testing machine coupled with digital image correlation technology at the temperature of 350 °C with applied strain rates ranging from 10<sup>-4</sup> s<sup>-1</sup> to 10<sup>-2</sup> s<sup>-1</sup>, as presented in Fig. 2a. Moreover, to directly observe the spatial behaviors of the PLC effect with Aramis software, a black and white contrast pattern should be sprayed on the surface of specimen prior to tests, which is shown as inset in the lower left corner. Then, the deformation characteristics of tensile specimen surfaces are captured continuously at a rate of 10 frames per second until rupture with the DIC, and a virtual grid 12 × 12 px as well as a 6 px step are used for the post-processing of the DIC. Figure 2b presents the true stress–strain curves under three different applied strain rates. Note that, these true stress–strain curves are converted from engineering stress–strain curves, which are obtained by coupling loading–time curves and strain–time curves. Specifically, the load–time curves are firstly obtained from the Gleeble 3500 testing machine. Then, these load–time curves are converted to engineering stress–time curves by Eq. (1). Moreover, during the tensile process, the displacement–time curves of *P*<sub>1</sub> and *P*<sub>2</sub> points (Fig. 1c) located at the ends of gauge length (10 mm) are obtained by the DIC. Subsequently, using the above displacement–time curves, the engineering strain–time curves are calculated by Eq. (2). Furthermore, through coupling the above engineering stress–time curves and engineering strain–time curves, the engineering stress–strain curves can be obtained. Finally, these engineering stress–strain curves are converted to the true stress–strain curves by Eqs. (3) and (4) [25]. In addition, each experimental test is repeated three times to ensure the reproducibility of the results.

$$\sigma_e = \frac{F}{A} \quad (1)$$

$$\varepsilon_e = \frac{\Delta L}{L} \quad (2)$$

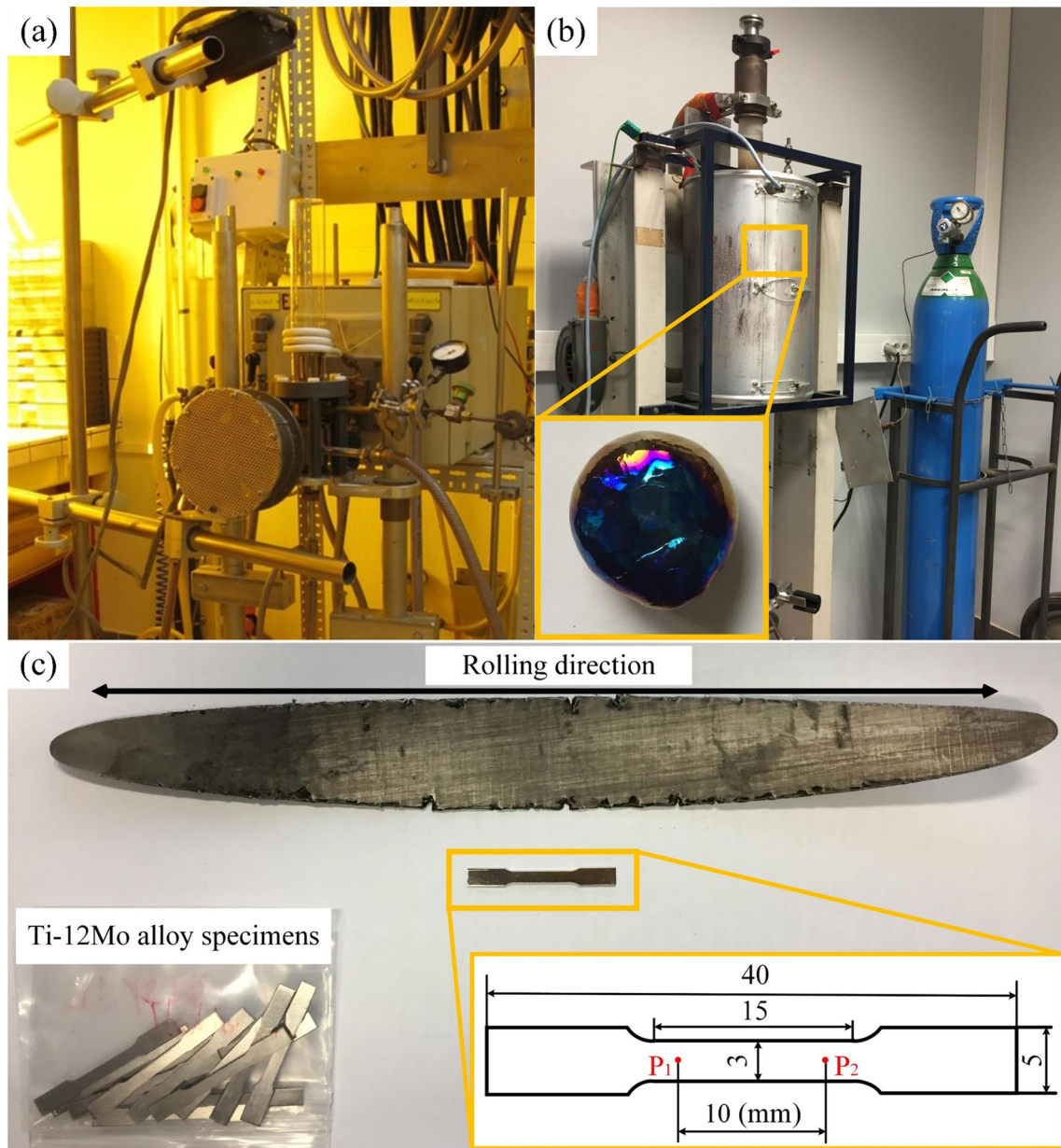


Fig. 1 Semi-levitation melting furnace (a), heat treatment equipment (b) and tensile specimens of Ti-12Mo alloy (c)

$$\sigma_t = \sigma_e(1 + \epsilon_e) \quad (3)$$

$$\epsilon_t = \ln(1 + \epsilon_e) \quad (4)$$

where  $\sigma_e$  is the engineering stress,  $F$  is the measured load,  $A$  is the original area of the cross section,  $\epsilon_e$  is the engineering strain,  $\Delta L$  is the increment of the original gauge length,  $L$  is the original gauge length,  $\sigma_t$  is true stress and  $\epsilon_t$  is the true strain.

### 3 Modified MC Constitutive Model and Parameter Calibration

#### 3.1 Modified MC Constitutive Model

In previous work [24], a MC constitutive model is utilized to simulate the spatiotemporal behaviors of the PLC effect in Ti-12Mo alloy tensile tests. Hereinto, the total tensor  $\xi$  is consisted of elastic part  $\xi^e$  and plastic part  $\xi^p$  [26]:

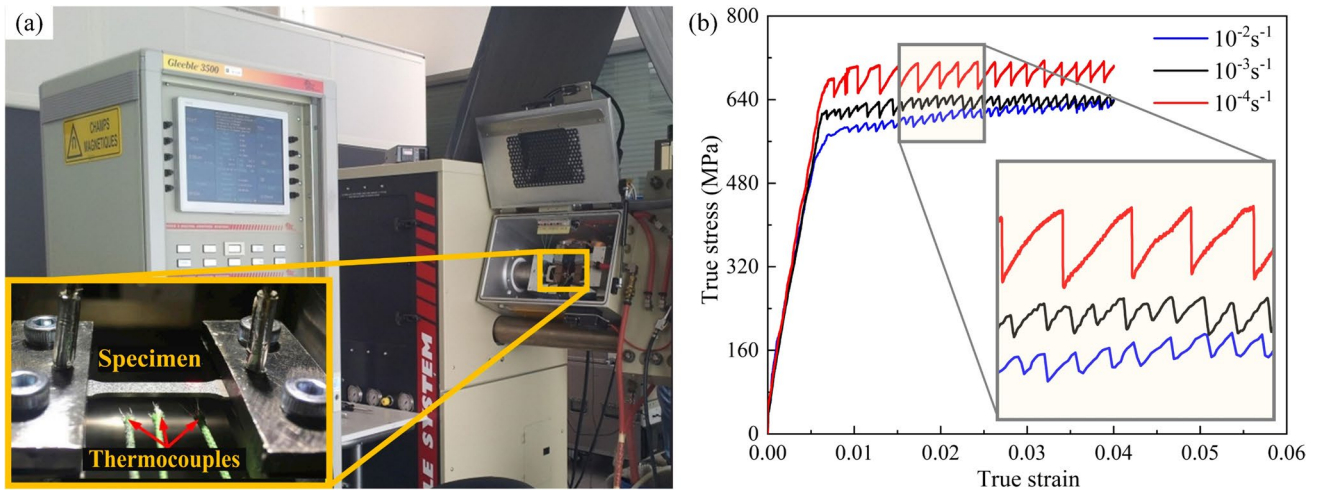


**Fig. 2** Gleeble 3500 testing machine with tensile specimens (a) and true stress–strain curves of Ti-12Mo alloy (b)

$$\varepsilon = \varepsilon^e + \varepsilon^p \quad (5)$$

$$\underline{\underline{\sigma}} = \underline{\underline{\zeta}} : \underline{\underline{\varepsilon}}^e \quad (6)$$

where  $\underline{\underline{\zeta}}$  denotes the fourth order tensor of elastic modulus,  $\underline{\underline{\sigma}}$  means the stress tensor.

Moreover, the yield function can be written as [27]:

$$f(\underline{\underline{\sigma}}, p, t_a) = \sigma_{eq} - R(p) - R_a(p, t_a) \quad (7)$$

$$\sigma_{eq} = \sqrt{\frac{3}{2} \underline{\underline{s}} : \underline{\underline{s}}} \quad (8)$$

where  $p$  denotes the equivalent plastic strain,  $t_a$  means the aging time,  $\sigma_{eq}$  is the equivalent stress, and  $\underline{\underline{s}}$  is the deviatoric part of the stress tensor. Note that  $R(p)$  means plastic strain hardening function and  $R_a(p, t_a)$  is the strain aging hardening term of the yield stress, which can be expressed as [24]:

$$R(p) = Q(1 - \exp(-bp)) \quad (9)$$

$$R_a(p, t_a) = R_0 + P_1 C_m (1 - \exp(-P_2 p^\alpha t_a^n)) \quad (10)$$

where  $Q$  and  $b$  are hardening parameters,  $R_0$  is related to the initial yield stress, and  $P_1 C_m$  is the stress resistance to dislocation motion due to the interaction with the  $\omega$  phase particles. Besides,  $P_2$ ,  $\alpha$  and  $n$  are the material parameters related to saturation rate, and the variations of  $t_a$  is calculated by following equations [28]:

$$\dot{t}_a = 1 - \frac{t_a}{t_w} \quad (11)$$

$$t_w = \frac{w}{\dot{p}} \quad (12)$$

where  $t_w$  represents the average waiting time of mobile dislocations,  $w$  means the increase of the plastic strain as the obstacles is overcome by all the stopped dislocations, and  $\dot{p}$  is the equivalent plastic strain rate which can be calculated by [29]:

$$\dot{p} = \dot{p}_0 \sinh \left( \frac{\langle f(\underline{\underline{\sigma}}, p, t_a) \rangle}{K} \right) \quad (13)$$

$$\langle f(\underline{\underline{\sigma}}, p, t_a) \rangle = \frac{\text{abs}(f(\underline{\underline{\sigma}}, p, t_a)) + f(\underline{\underline{\sigma}}, p, t_a)}{2} \quad (14)$$

where  $\text{abs}(f(\underline{\underline{\sigma}}, p, t_a))$  denotes the absolute value of  $f(\underline{\underline{\sigma}}, p, t_a)$ ,  $\dot{p}_0$  and  $K$  are material parameters.

Note that, the equivalent plastic strain rate  $\dot{p}$  is nearly constant when the strain is less than the critical plastic strain of the PLC effect. Therefore,  $t_a$  can be also rewritten as the function of  $p$  [29]:

$$t_a(p) = \frac{w}{\dot{p}} \left( 1 - \exp\left(-\frac{p}{w}\right) \right) + \frac{R_0}{E\dot{p}} \exp\left(-\frac{p}{w}\right) \quad (15)$$

Furthermore, coupling the above formulas, the stress homogeneous solution can be obtained:

$$\sigma = K \arcsin h \left( \frac{\dot{p}}{\dot{p}_0} \right) + R_0 + Q(1 - \exp(-bp)) + P_1 C_m (1 - \exp(-P_2 p^\alpha t_a(p)^n)) \quad (16)$$

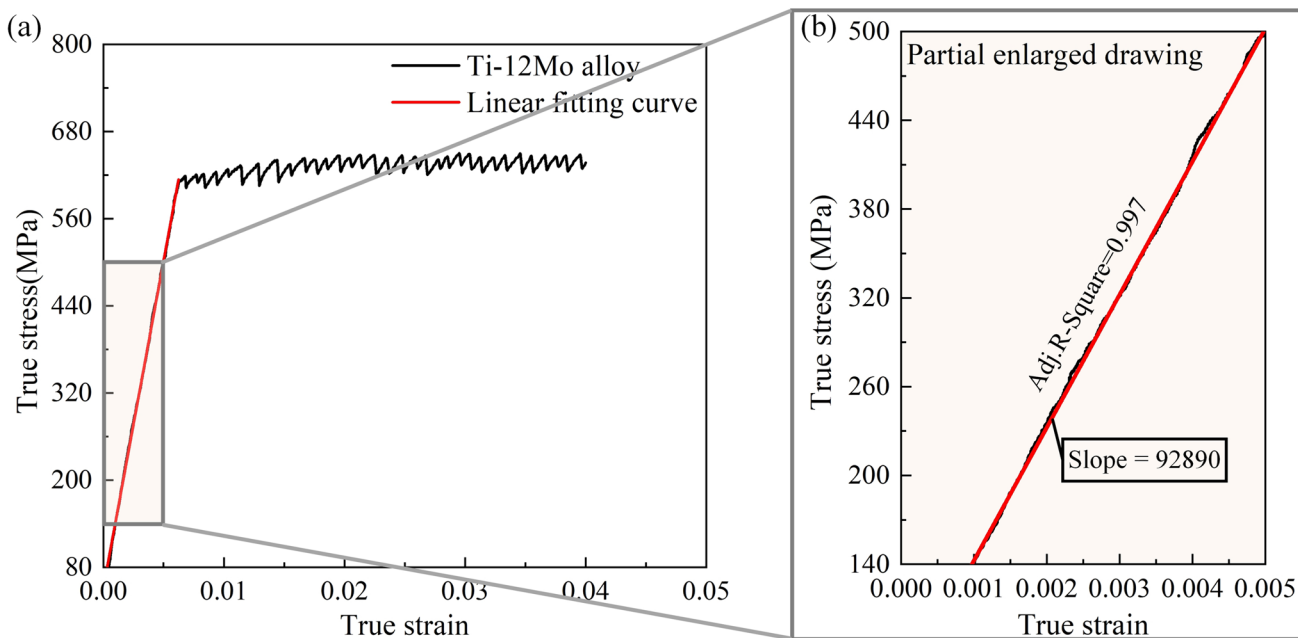


Fig. 3 Fitting the elastic part of Ti-12Mo alloy stress–strain curve (a) with partial enlarged drawing (b)

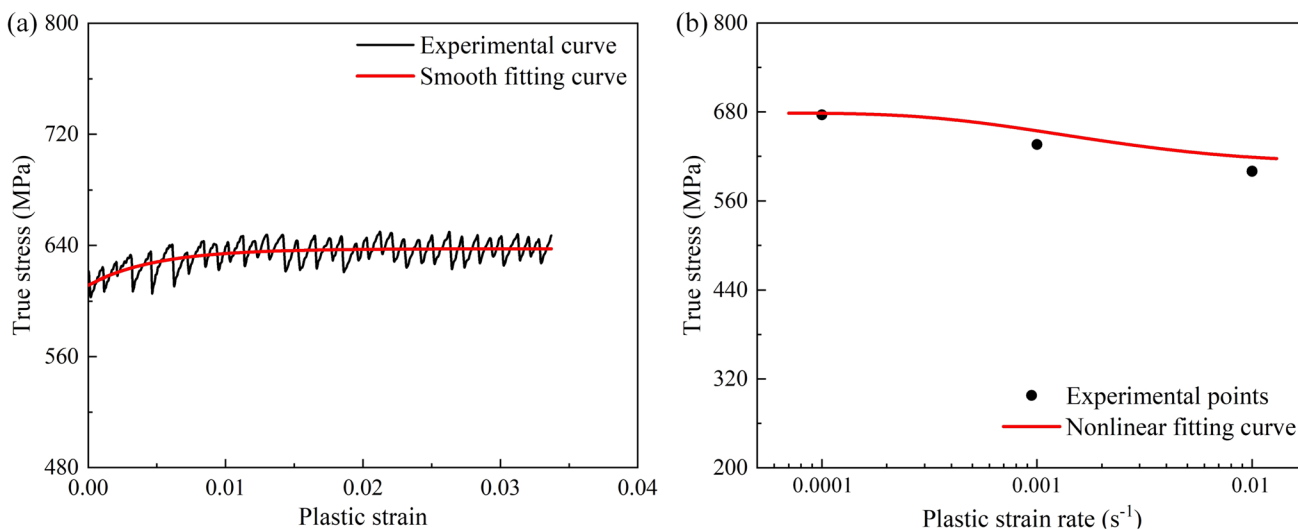


Fig. 4 Fitting the plastic part of strain–stress curve (a) and negative strain rate sensitivity curve (b) of Ti-12Mo alloy

In the aforementioned MC model,  $C_m$  and  $w$  are regarded as constant material parameters. In fact, however, these parameters are proved to be strain dependent parameters [15, 30]. Therefore, in this work, to improve the MC model, the above two parameters are respectively defined as linear and nonlinear functions of equivalent plastic strain, which are written as:

$$C_m(p) = C_{m1}p + C_{m2} \tag{17}$$

$$w(p) = w_1(p)^\beta + w_2 \tag{18}$$

where  $C_{m1}$ ,  $C_{m2}$ ,  $w_1$ ,  $w_2$  and  $\beta$  are constant parameters.

Finally, embedding Eqs. (17) and (18) into Eqs. (15) and (16), the explicit expression of  $t_a$  and the stress homogeneous solution can be rewritten as:

$$t_a(p) = \frac{w_1(p)^\beta + w_2}{\dot{p}} \left( 1 - \exp\left(-\frac{p}{w_1(p)^\beta + w_2}\right) \right) + \frac{R_0}{E\dot{p}} \exp\left(-\frac{p}{w_1(p)^\beta + w_2}\right) \quad (19)$$

$$\sigma = K \arcsin h\left(\frac{\dot{p}}{\dot{p}_0}\right) + R_0 + Q(1 - \exp(-bp)) + P_1(C_{m1}(p) + C_{m2})(1 - \exp(-P_2 p^\alpha t_a(p)^n)) \quad (20)$$

## 3.2 Material Parameter Calibration

### 3.2.1 Elastic Parameter Calibration

Before using the above modified MC model of Ti-12Mo alloy, 16 material parameters, including 2 elastic and 14 plastic parameters, need to be identified. Hereinto, for elastic parameters, a linear fitting method is employed to obtain the Young's modulus ( $E$ ) by fitting the experimental stress–strain curve obtained at the strain rate of  $1 \times 10^{-3} \text{ s}^{-1}$  in the stress range (100–400 MPa), as shown in Fig. 3a. It can be observed from Fig. 3b the value of  $E$  is 92.890 GPa and the linear fitting curve is highly consistent with the experimental one (adjusted R-squared = 0.997). Moreover, the Poisson's ratio ( $\nu$ ) of Ti-12Mo alloy is 0.33 [31].

### 3.2.2 Plastic Parameter Calibration

For the plastic part of Ti-12Mo alloy, using Eq. (9) and non-linear curve fitting method,  $Q$  and  $b$  are identified by fitting the plastic part of true stress–plastic strain curve (Fig. 4a),

**Table 1** Material parameters for modeling the PLC effect in Ti-12Mo alloy

Parameters	Units	Values
$E$	GPa	92.890
$\nu$	–	0.33 [31]
$R_0$	MPa	570
$Q$	MPa	27.075
$b$	–	220.458
$K$	MPa	15 [24]
$\dot{p}_0$	$\text{s}^{-1}$	0.05 [24]
$P_1$	MPa	85
$P_2$	$\text{s}^{-n}$	15 [24]
$C_{m1}$	%	3
$C_{m2}$	%	0.9
$\alpha$	–	0.36 [24]
$\beta$	–	0.68 [30]
$w_1$	–	$2.16 \times 10^{-3}$ [30]
$w_2$	–	$3.63 \times 10^{-5}$ [30]
$n$	–	0.66 [32]

whose values are 27.075 MPa, 220.458 respectively. Then,  $w_1$ ,  $w_2$ ,  $\beta$  and  $n$  are respectively  $2.16 \times 10^{-3}$ ,  $3.63 \times 10^{-5}$ , 0.68 and 0.66, referring to the literature [30, 32]. Moreover, the values of viscous ( $K$ ,  $\dot{p}_0$ ) and aging ( $P_2$ ,  $\alpha$ ) parameters are respectively 15 MPa,  $0.05 \text{ s}^{-1}$ ,  $15 \text{ s}^{-n}$ , 0.36, which are received from the literature [24]. Furthermore, to calibrate the remaining parameters  $R_0$ ,  $P_1$ ,  $C_{m1}$ ,  $C_{m2}$ , uniaxial tensile tests are conducted at 350 °C with three different applied strain rates from the order of  $10^{-4} \text{ s}^{-1}$  to  $10^{-2} \text{ s}^{-1}$  (Fig. 2d). Subsequently, the true stress–strain curves with different strain rates are smoothed. After that, the true stress values of different strain rates at  $p=0.02$  are obtained from these

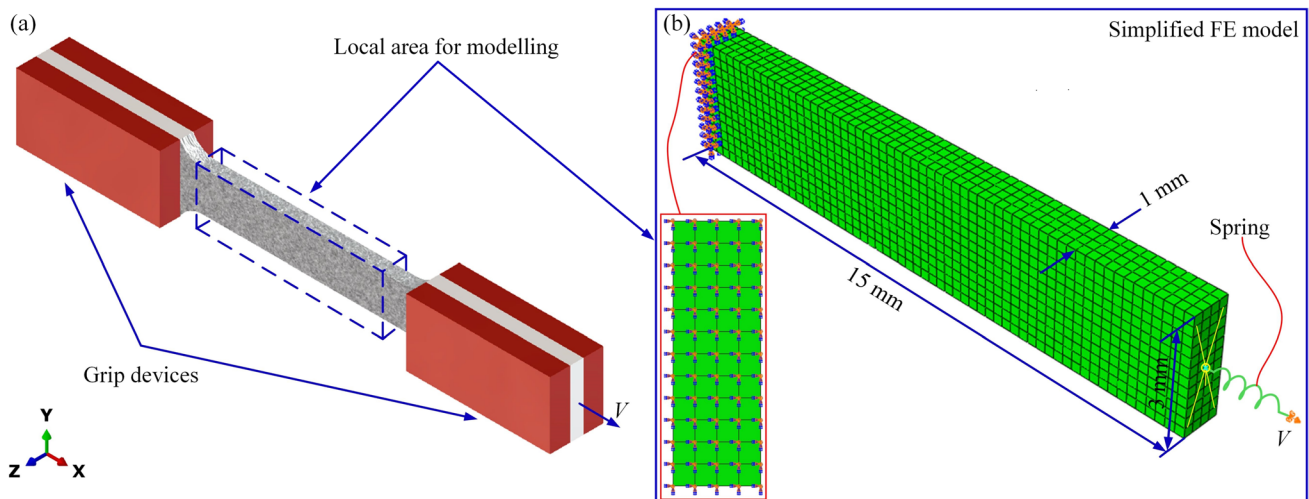


**Fig. 5** Diagram of Ti-12Mo alloy uniaxial tensile tests (a) and its simplified 3D FE model (b)

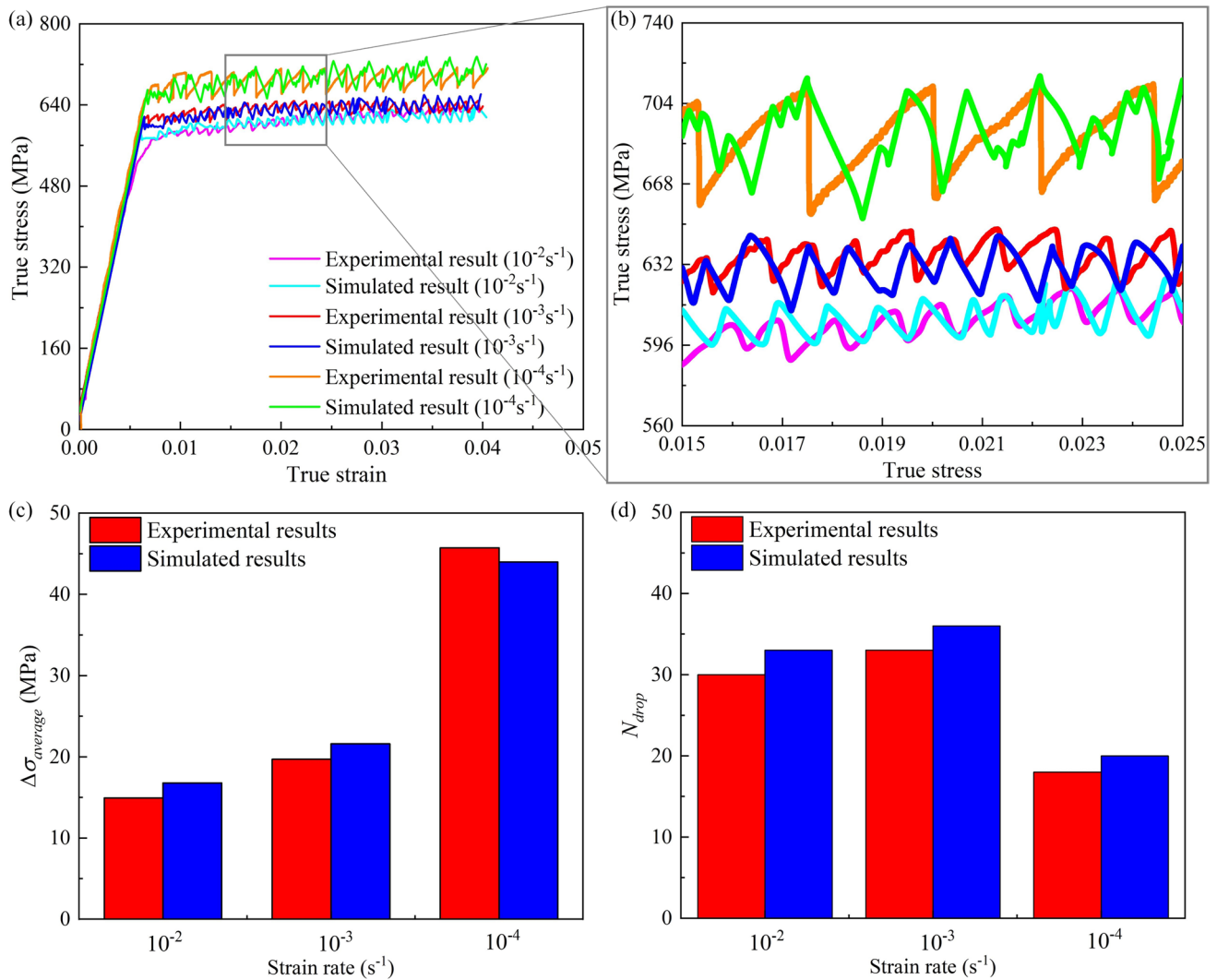


**Fig. 6** Comparisons of experimental and simulated results in terms of stress–strain curves (a), their partial enlarged drawing (b),  $\Delta\sigma_{\text{average}}$  (c) and  $N_{\text{drop}}$  (d) during the tensile process

smoothed true stress–strain curves and depicted as black points in Fig. 4b. Finally, using Eq. (20) and Levenberg Marquardt algorithm, the values of the above 4 remaining parameters can be determined by fitting these points with the maximum error less than 4%, whose values are respectively 570 MPa, 85 MPa, 3% and 0.9%. Besides, a summary of calibrated 16 material parameters are listed in Table 1.

## 4 Improved FE Model and Experimental Verification

### 4.1 Improved FE Model

The improved FE model is mainly developed by defining material, geometry, boundary conditions, and mesh under

ABAQUS 6.14 software environment. For the material part, to accurately predict the spatiotemporal behaviors of the PLC effect in Ti-12Mo alloy uniaxial tensile tests, the above modified MC constitutive model with calibrated parameters is embedded by using a UMAT subroutine. Moreover, Fig. 5a presents the diagram of Ti-12Mo alloy uniaxial tensile tests. Due to the fact that the deformation mainly occurs at the center of tensile specimens, the geometry of the FE model is simplified as Fig. 5b, which can effectively ensure simulation accuracy and reduce computational time. Furthermore, unlike the FE model developed in previous work [24], the effect of machine stiffness is taken into consideration in the improved model and an elastic spring with the value of 20,000 N/mm is applied on the right side of the specimen. Subsequently, a constant velocity is applied to the right end of the spring and an encastre constraint is

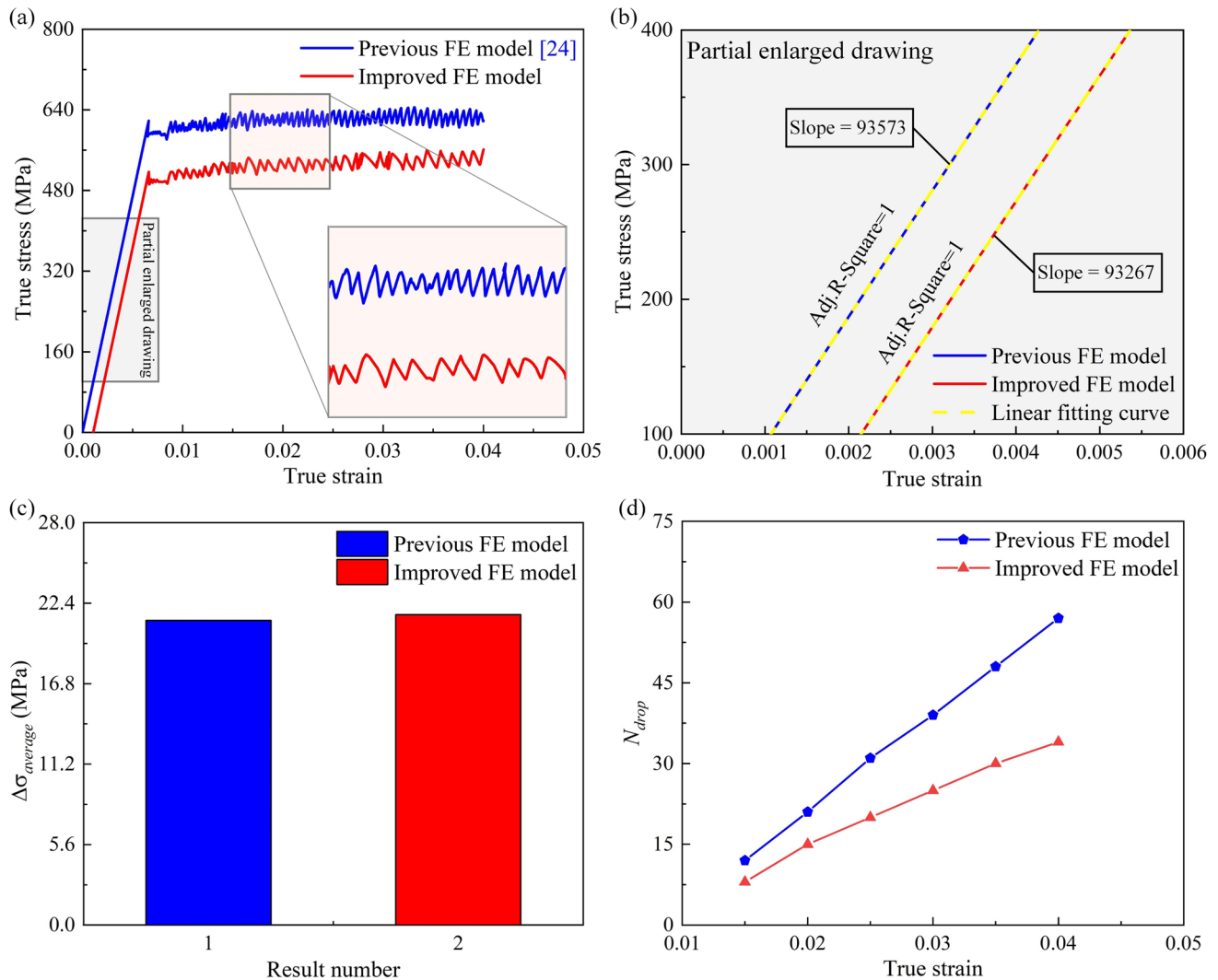


**Fig. 7** Comparisons of stress–strain curves (a), Young’s modulus (b),  $\Delta\sigma_{average}$  (c), and  $N_{drop}$  (d)

adopted on the left side of the specimen to restrict all the displacements and rotations. Finally, for the mesh part, to avoid zero modes, eight node hexahedral linear reduced integral elements (C3D8R) with the mesh size of  $0.25 \times 0.25 \times 0.25$  mm<sup>3</sup> are employed in the FE model.

## 4.2 Experimental Verification

To verify the validity of the above improved FE model embedded with the modified MC model, the FE model is calculated by a computer with Intel core i7-10700 K and 64 GB RAM, and its simulated stress–strain curves are compared with experimental ones at three different strain rates from the order of  $10^{-4}$  s<sup>-1</sup> to  $10^{-2}$  s<sup>-1</sup> (Fig. 6a). For the stress levels of elasticity and plasticity parts, it can be observed that the experimental results can be well predicted by the FE model. Moreover, Fig. 6c, d presents the comparison of

simulation and experimental results in terms of the average stress drop magnitude ( $\Delta\sigma_{average}$ ) and the number of stress drops ( $N_{drop}$ ) during the tensile process. Hereinto, the average stress drop magnitude is calculated by  $\Delta\sigma_{average} = \sum_{i=1}^n \Delta\sigma_i / n$  [33]. It can be seen that simulated results show good agreement with experimental ones in terms of  $\Delta\sigma_{average}$  and  $N_{drop}$  with the maximum error less than 10%. Therefore, the improved FE model embedded with the modified MC model established in this paper is effective, and its simulated results are reliable.



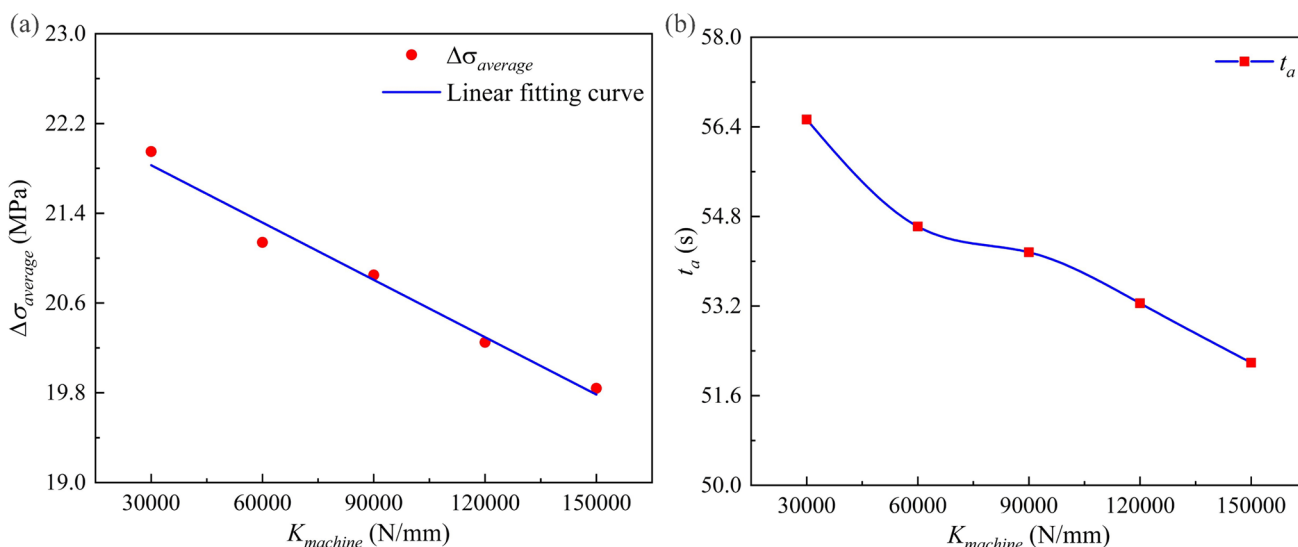


Fig. 8 Evolutions of  $\Delta\sigma_{average}$  (a) and  $t_a$  (b) with different  $K_{machine}$

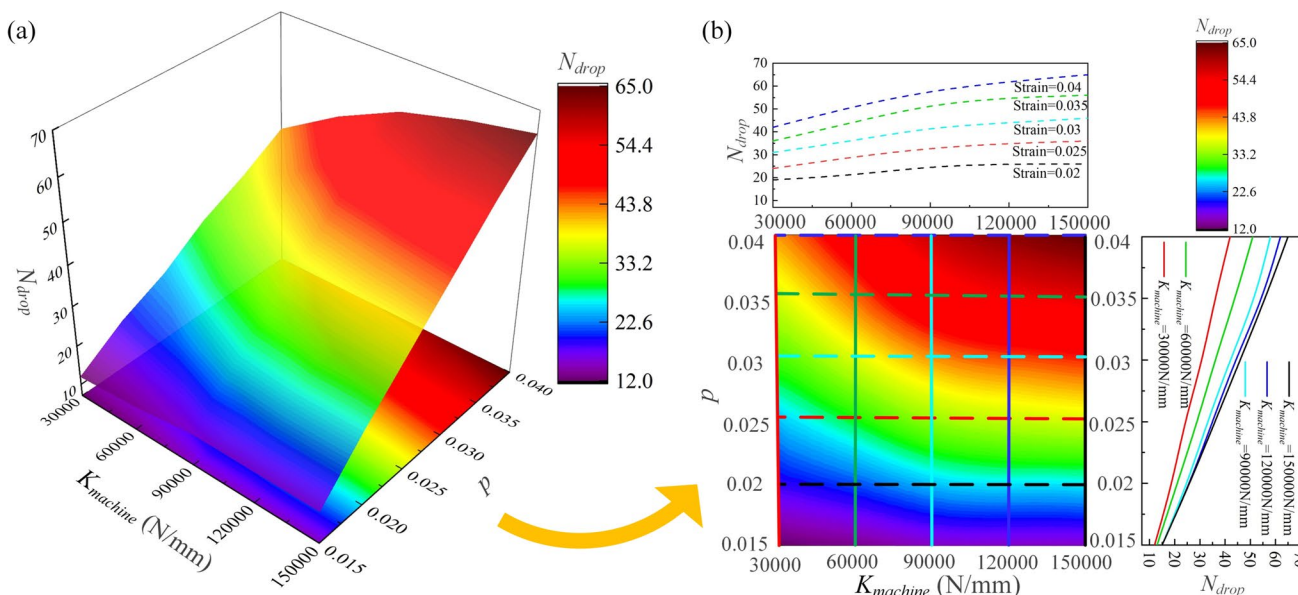


Fig. 9 Variations of  $N_{drop}$  with different  $K_{machine}$  and  $p$  in a 3D surface form (a) and its contour plot with some fundamental evolution laws of  $N_{drop}$  (b)

## 5 Results and Discussion

### 5.1 Comparisons of Simulated PLC Effect Using Different FE Models

Figure 7a presents the comparison of the simulated stress–strain curve obtained by the above improved FE model and the one predicted by previous FE model [24]. Note that, their tensile velocities are the same (0.01 mm/s) and the former one is shifted – 100 MPa along the Y-axis

to avoid overlapping curves. Although these stress–strain curves are numerically obtained by the same finite element software (ABAQUS 6.14), however, the curve calculated by the previous FE model ignores the effect of machine stiffness and the variations of  $C_m$  and  $w$  in the MC constitutive model. Then, using quantitative analysis, Fig. 7b compares the simulated Young’s modulus of two different FE models. Note that, the Young’s modulus value is obtained by fitting the simulated stress–strain curves in the linear part of the stress range 100–400 MPa. It can be obtained that the simulated Young’s modulus values of improved and previous

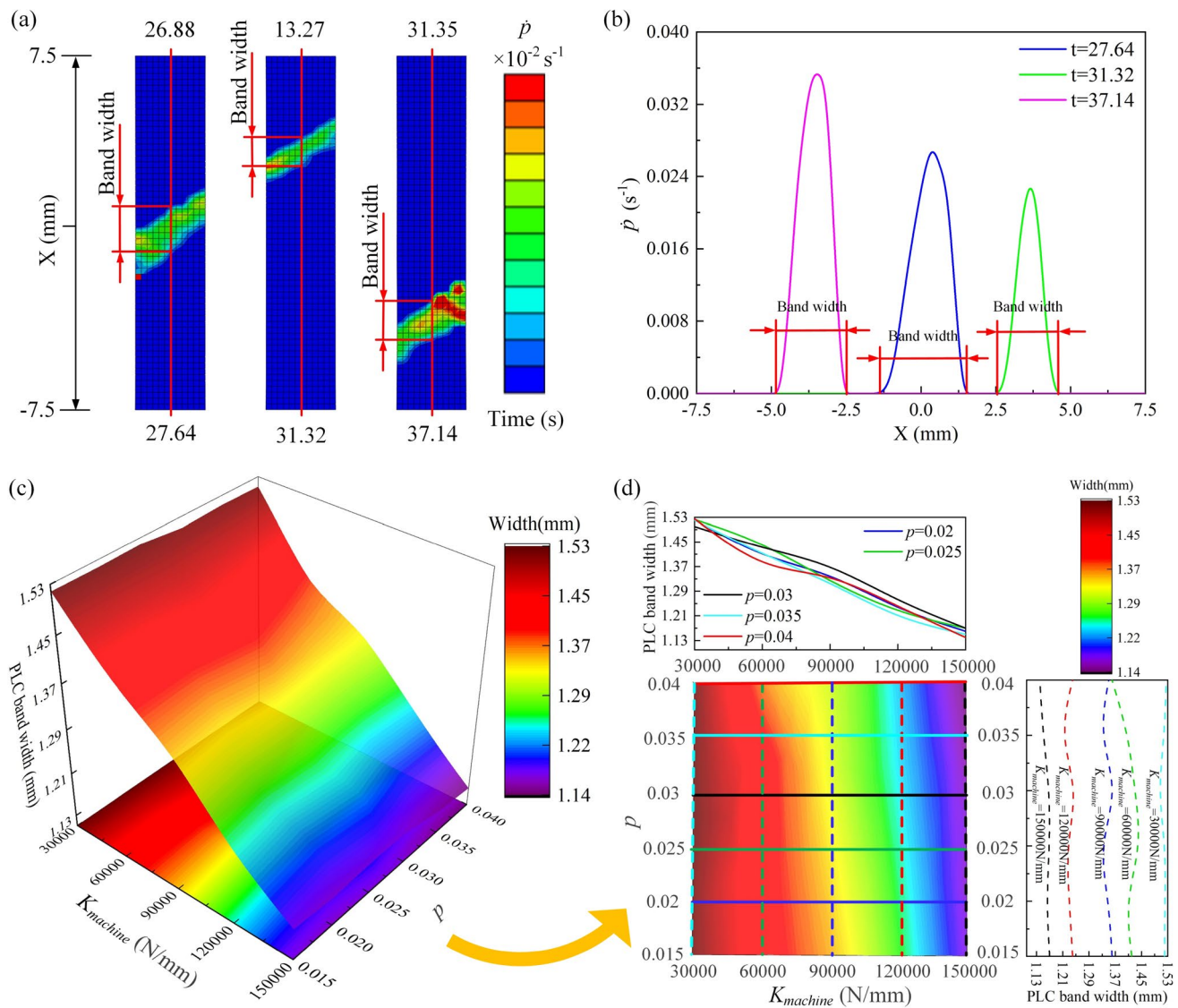


**Fig. 10** Measurement schematic diagram of the PLC band width (a), distributions of  $\dot{p}$  on the central axis of the specimen along the tensile direction (b), variations of the PLC band width with different  $K_{\text{machine}}$

and  $p$  in a 3D surface form (c) and its contour plot with some fundamental evolution laws of the PLC band width (d)

FE models are 93.267 GPa and 93.573 GPa, as well as both of their adjusted R-squared are 1. Compared with experimental value of Young's modulus (92.890 GPa) obtained in Sect. 3.2.1, it can be found that the errors between simulated and experimental results are all less than 0.8%. Therefore, it can be deduced that both of above two FE models can well predict the elastic deformation of Ti-12Mo alloy. Furthermore, Fig. 7c compares the simulated  $\Delta\sigma_{\text{average}}$  values of above two FE models. It can be found that the  $\Delta\sigma_{\text{average}}$  values of improved and previous FE models are respectively 21.6 MPa and 21.2 MPa, and their errors between simulated and experimental results are all less than 9.65%. Finally, Fig. 7d compares the simulated  $N_{\text{drop}}$  values of above two FE models. It can be seen that their simulated  $N_{\text{drop}}$  show the

similar evolution trend, which generally increase as increasing strain. However, it can be found that the simulated  $N_{\text{drop}}$  value of the improved FE model is significantly less than the one of the previous FE model. This phenomenon indicates that the stress drop frequency of the improved FE model considering the effect of machine stiffness and the variations of  $C_m$  and  $w$  is lower the one of the previous FE model. Combined Fig. 6d and Fig. 7d, it can be concluded that the improved FE model is more accuracy than the previous one in predicting the stress drop frequency of the PLC effect in Ti-12Mo alloy.

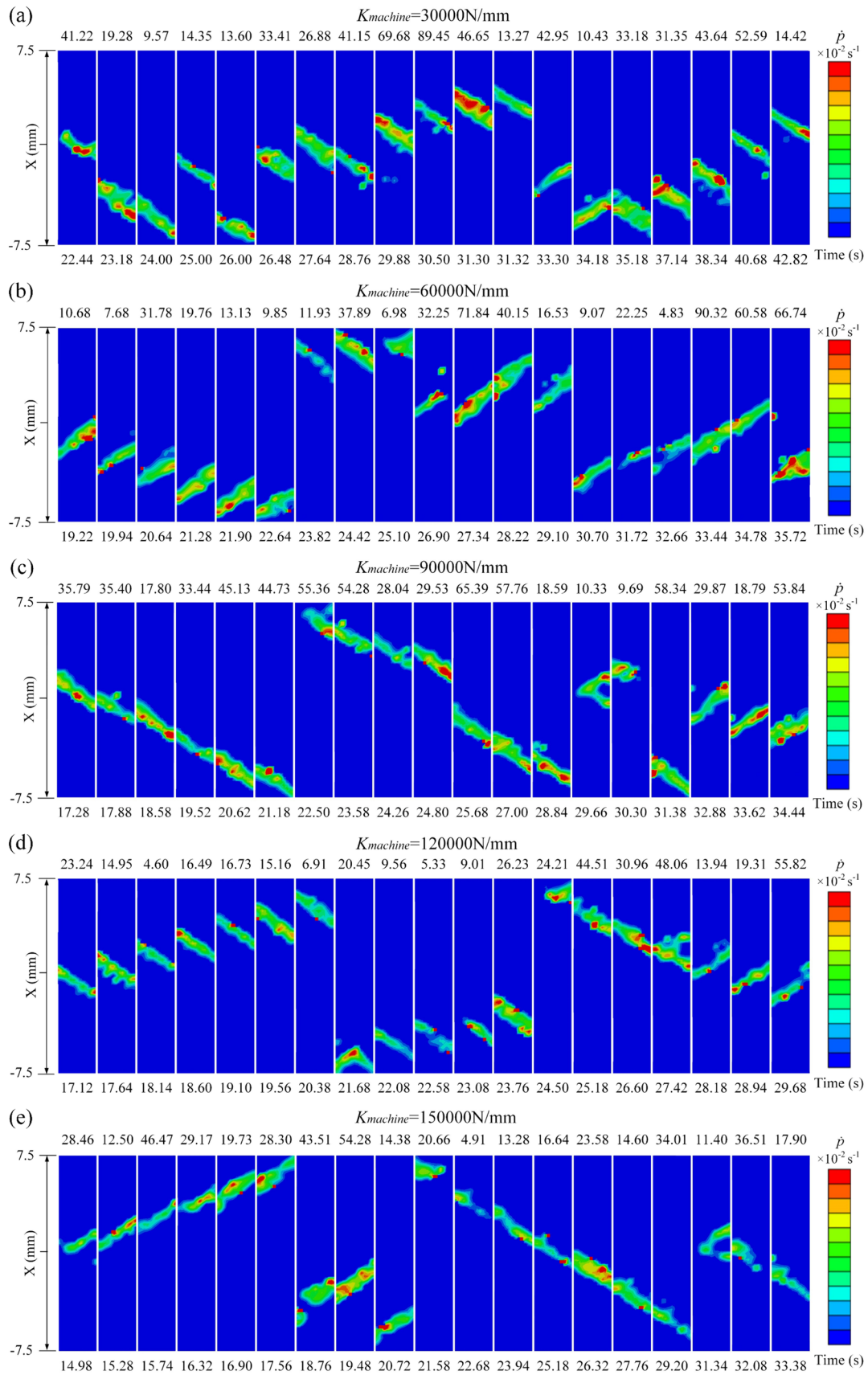


Fig. 11 Propagations of the PLC band with  $K_{machine}=30,000\text{ N/mm}$  (a),  $60,000\text{ N/mm}$  (b),  $90,000\text{ N/mm}$  (c),  $120,000\text{ N/mm}$  (d) and  $150,000\text{ N/mm}$  (e)

## 5.2 Machine Stiffness Effects on Temporal Behaviors of The PLC Effect

To simulate the effects of machine stiffness on the temporal characteristics of the PLC effect in Ti-12Mo alloy tensile process, a series of machine stiffnesses characterized by  $K_{machine} = \{30,000, 60,000, 90,000, 120,000, 150,000\}$  (N/mm) are employed.

### 5.2.1 Influence of Machine Stiffness on Average Stress Drop Magnitude

Figure 8a presents the variation of  $\Delta\sigma_{average}$  with different  $K_{machine}$ . It can be seen that the value of  $\Delta\sigma_{average}$  generally decreases from 21.95 MPa to 19.84 MPa as the  $K_{machine}$  increases from 30,000 N/mm to 150,000 N/mm. This phenomenon shows a similar evolution trend reported by Guillermin et al. [34], who investigated the PLC effect of nickel-based superalloy in high temperature tensile tests. This result is mainly related to the variation of  $t_a$ . Specifically, a relatively higher value of  $K_{machine}$  leads to a lower value of  $t_a$  calculated at  $p=0.04$  (Fig. 8b), further decreasing the concentration of  $\omega$  phase particles around the mobile dislocations, thereby resulting in a weaker interaction between  $\omega$  phase particles and mobile dislocations, and eventually causing the decrease of  $\Delta\sigma_{average}$ .

### 5.2.2 Influence of Machine Stiffness on the Number of Stress Drops

Figure 9a shows the variations of  $N_{drop}$  with different  $K_{machine}$  and  $p$  in a 3D surface form. Unlike  $\Delta\sigma_{average}$ , it can be observed that the value of  $N_{drop}$  increases as increasing  $K_{machine}$  and  $p$ . Moreover, to quantitatively analyze the variations of  $N_{drop}$ , the projection of Fig. 9a with some fundamental evolution laws of  $N_{drop}$  are depicted as Fig. 9b. It can be found from Fig. 9b that as  $p=0.04$ , the maximum value of  $N_{drop}$  (about 42) at  $K_{machine}=30,000$  N/mm is nearly 1.55 times smaller than the one (about 65) at  $K_{machine}=150,000$  N/mm. This finding indicates that increasing machine stiffness will lead to the increase of stress drop frequency. This phenomenon is mainly attributed to the fact that increasing  $K_{machine}$  results in the decrease of  $t_a$ , further reducing the concentration of  $\omega$  phase particles around mobile dislocations, thereby causing the decrease of pinning strength and  $t_w$ , and eventually leading to the increment of stress drop frequency. In addition, it can be observed that as  $K_{machine}=150,000$  N/mm, the value of  $N_{drop}$  at  $p=0.04$  is nearly 2.5 times larger than the one (about 26) at  $p=0.02$ , which indicates that increasing strain leads to the increase of stress drop frequency. This finding is highly consistent

with the results reported by Luo et al. [35], who investigate the number variation of stress drops per unit time in Ti-xMo alloys tensile tests by using a digital image correlation method.

## 5.3 Machine Stiffness Effects on Spatial Behaviors of the PLC Effect

### 5.3.1 Influences of Machine Stiffness on the PLC Band Width

Figure 10a describes the measurement schematic diagram of the PLC band width. It can be seen that the PLC band width is defined as the distance between the two closest extremum points on opposite sides of the PLC band and measured on the central axis of the specimen along the tensile direction [36]. For further quantitative analysis, the distributions of  $\dot{p}$  values on the central axis of the specimen along the tensile direction are obtained from the post-processing of ABAQUS 6.14 software, as shown in Fig. 10b. Figure 10c shows the variations of the PLC band width with different  $K_{machine}$  and  $p$  in a 3D surface form. It can be observed that unlike the small effect of  $p$ , the PLC band width sharply decrease with the increase of  $K_{machine}$ . Furthermore, to quantitatively reflect the variations of the PLC band width, the projection of Fig. 10c with some fundamental evolution laws of the PLC band width are depicted as Fig. 10d. It can be observed that the PLC band width value at  $K_{machine}=30,000$  N/mm (about 1.53 mm) is nearly 1.34 times larger than the one at  $K_{machine}=150,000$  N/mm (about 1.14 mm). This is mainly because a relatively higher  $K_{machine}$  leads to a lower value of  $t_a$ , further decreasing the concentration of  $\omega$  phase particles around the mobile dislocations, then resulting in a weaker driving force of band nucleation, and eventually causing the decrease of the PLC band width. This explanation can be supported by the work of Shabadi et al. [37], who found that the decrease of solute content in matrix makes the driving force of band nucleation become less, and further resulting in thinner bands in 7020 alloy. Besides, this finding is highly consistent with the results reported by Liu et al. [38], who investigated the influence of  $\gamma'$  phase content on the PLC band width in Ni-Co based alloy tensile tests and found that the PLC band width of 30%  $\gamma'$  phase is larger than the one of 5%  $\gamma'$  phase.

### 5.3.2 Influences of Machine Stiffness on the Propagation of the PLC Band

Figure 11 presents the propagation characteristics of the PLC band with different  $K_{machine}$ . Hereinto, to reveal a maximum contrast, an independent color scale is used for each frame with the corresponding maximum strain rate and time value marked above and below each frame. It can be observed that

the propagation of the PLC band with different  $K_{machine}$  all belong to A + B type, which contains continuous and hopping propagations. Moreover, it can be also found that the propagation continuity of the PLC band obviously increases with the increase of  $K_{machine}$ . This phenomenon is highly consistent with the results reported by Tretyakova et al. [39], who investigated the effect of machine stiffness on the variation of the PLC propagation in Al–Mg alloy tensile tests by using a digital image correlation method. This result is mainly related to the variation of spatial coupling force. Specifically, increasing  $K_{machine}$  results in the decrease of  $t_a$ , further leading to the decreases of  $\omega$  phase concentration and the pinning strength between  $\omega$  phase particles and mobile dislocations. Then, a lower pinning strength will lead to the decrease of  $t_w$  and provide a less time for the plastic relaxation of the internal stress, thereby causing a greater spatial coupling force, and finally making the PLC band tend to be continuous propagation with increasing machine stiffness. This explanation can be supported by the work of Cai et al. [36], who found that the spatially continuous propagation requires higher coupling force than discontinuous propagation in the PLC effect of Al–Mg alloy.

## 6 Conclusions

In this paper, an improved FE model embedded with the modified MC constitutive model is developed to investigate the influence of machine stiffness on the spatiotemporal behaviors of the PLC effect in Ti-12Mo alloy tensile tests and verified by experiments. The following conclusions are achieved:

- (1) Compared with the previous FE model, the improved one considering the effects of machine stiffness and strain shows essentially the same simulation accuracy in terms of Young's modulus and average stress drop magnitude and a higher simulation accuracy in term of stress drop frequency. These results indicate that the improved FE model has a better prediction effect in the temporal behaviors of the PLC effect during the Ti-12Mo alloy tensile process.
- (2) For the temporal aspects of the PLC effect, the value of average stress drop magnitude slightly decreases from 21.95 MPa to 19.84 MPa as the machine stiffness increases from 30,000 N/mm to 150,000 N/mm, which is mainly related to the weak interaction between  $\omega$  phase particles and mobile dislocations. Moreover, unlike the variation of stress drop magnitude, the number of stress drops increases with the increase of machine stiffness and strain, which is mainly attributed to the decrease of aging time.
- (3) For the spatial aspects of the PLC effect, the PLC band width decreases from 1.53 mm to 1.14 mm as the machine stiffness increases from 30,000 N/mm to 150,000 N/mm, which is mainly attributed to the decrease of driving force for band nucleation. Moreover, although the continuous and hopping propagations of the PLC band are observed with different machine stiffness, its propagation continuity obviously increases with the increase of machine stiffness, which is mainly related to the increase of spatial coupling force.

**Acknowledgements** This work was supported by the National Natural Science Foundation of China (grant no. 52301166). Moreover, the authors wish to thank Prof. S. Thuillier and Prof. P. Castany for their help and assistance in conducting the experimental work.

**Author Contribution** SL: Conceptualization, Methodology, Writing-original draft. LX: Investigation, Software, Validation, Writing-original draft. JJ: Data curation, Writing-review & editing. JL: Data curation, Writing-review & editing. LZ: Supervision, Writing-review & editing.

## Declarations

**Conflict of interests** The authors declare that they have no known competing financial interests or personal relationships that could have appeared to influence the work reported in this paper.

## References

1. J.G. Lee, D.G. Lee, J. Mater. Res. Technol. **25**, 7119 (2023). <https://doi.org/10.1016/j.jmrt.2023.07.104>
2. C. Suwanpreecha, S. Songkuea, P. Wangjina, M. Tange, W. Pongsaksawad, A. Manonukul, Met. Mater. Int. **29**, 3298 (2023). <https://doi.org/10.1007/s12540-023-01454-2>
3. P. Kumar, N.K. Jain, S. Gupta, Met. Mater. Int. **30**, 646 (2024). <https://doi.org/10.1007/s12540-023-01540-5>
4. S. Ahmad, A. Alankar, V. Tathavadkar, K. Narasimhan, Met. Mater. Int. (2024). <https://doi.org/10.1007/s12540-023-01619-z>
5. S.C. Ren, T.F. Morgeneyer, M. Mazière, S. Forest, G. Rousselier, Int. J. Plast. **136**, 102880 (2021). <https://doi.org/10.1016/j.ijplas.2020.102880>
6. R. Jaisawal, V. Gaur, S. Ahmed, Int. J. Fatigue **174**, 107712 (2023). <https://doi.org/10.1016/j.ijfatigue.2023.107712>
7. G. Ananthakrishna, M.C. Valsakumar, J. Phys. D Appl. Phys. **15**, L171 (1982). <https://doi.org/10.1088/0022-3727/15/12/003>
8. R. Sarmah, G. Ananthakrishna, Acta Mater. **91**, 192 (2015). <https://doi.org/10.1016/j.actamat.2015.03.027>
9. L.P. Kubin, Y. Estrin, Acta Metall. **33**, 397 (1985). [https://doi.org/10.1016/0001-6160\(85\)90082-3](https://doi.org/10.1016/0001-6160(85)90082-3)
10. S. Kok, M.S. Bharathi, A.J. Beaudoin, C. Fressengeas, G. Ananthakrishna, L.P. Kubin, M. Lebyodkin, Acta Mater. **51**, 3651 (2003). [https://doi.org/10.1016/S1359-6454\(03\)00114-9](https://doi.org/10.1016/S1359-6454(03)00114-9)
11. P.G. McCormick, Acta Metall. **36**, 3061 (1988). [https://doi.org/10.1016/0001-6160\(88\)90043-0](https://doi.org/10.1016/0001-6160(88)90043-0)
12. S. Zhang, P.G. McCormick, Y. Estrin, Acta Mater. **49**, 1087 (2001). [https://doi.org/10.1016/S1359-6454\(00\)00380-3](https://doi.org/10.1016/S1359-6454(00)00380-3)
13. S. Graff, S. Forest, J.L. Strudel, C. Prioul, P. Pilvin, J.L. Béchede, Scr. Mater. **52**, 1181 (2005). <https://doi.org/10.1016/j.scriptamat.2005.02.007>

14. A. Benallal, T. Berstad, T. Børvik, O.S. Hopperstad, I. Koutiri, R.N.D. Codes, *Int. J. Plast.* **24**, 1916 (2008). <https://doi.org/10.1016/j.ijplas.2008.03.008>
15. T. Böhlke, G. Bondár, Y. Estrin, M.A. Lebyodkin, *Comput. Mater. Sci.* **44**, 1076 (2009). <https://doi.org/10.1016/j.commatsci.2008.07.036>
16. M. Mazière, A. Mortensen, S. Forest, *Philos. Mag.* **101**, 1471 (2021). <https://doi.org/10.1080/14786435.2021.1919331>
17. J. Xu, O.S. Hopperstad, B. Holmedal, T. Berstad, T. Mánik, K. Marthinsen, *Int. J. Plast.* **169**, 103706 (2023). <https://doi.org/10.1016/j.ijplas.2023.103706>
18. B. Klusemann, G. Fischer, T. Böhlke, B. Svendsen, *Int. J. Plast.* **67**, 192 (2015). <https://doi.org/10.1016/j.ijplas.2014.10.011>
19. M. Mucha, B. Weisto, J. Pamin, *Materials* **15**, 4327 (2022). <https://doi.org/10.3390/ma15124327>
20. C. Moon, S. Thuillier, J. Lee, M.G. Lee, *J. Alloys Compd.* **856**, 158180 (2021). <https://doi.org/10.1016/j.jallcom.2020.158180>
21. L.Z. Mansouri, J. Coër, S. Thuillier, H. Laurent, P.Y. Manach, *Int. J. Mater. Form.* **13**, 687 (2020). <https://doi.org/10.1007/s12289-019-01511-5>
22. S. Patra, S. Dhar, S.K. Acharyya, *Aust. J. Struct. Eng.* **23**, 214 (2022). <https://doi.org/10.1080/13287982.2022.2046317>
23. Y.F. Wang, J.R. Xing, Y.X. Zhou, C. Kong, H.L. Yu, *J. Alloys Compd.* **942**, 169044 (2023). <https://doi.org/10.1016/j.jallcom.2023.169044>
24. S.Y. Luo, Y.X. Jiang, S. Thuillier, P. Castany, L.C. Zeng, *Met. Mater. Int.* **29**, 269 (2023). <https://doi.org/10.1007/s12540-022-01226-4>
25. H.D. Kweon, J.W. Kim, O. Song, D. Oh, *Nucl. Eng. Technol.* **53**, 647 (2021). <https://doi.org/10.1016/j.net.2020.07.014>
26. S. Graff, S. Forest, J.L. Strudel, C. Prioul, P. Pilvin, J.L. Béchade, *Mater. Sci. Eng. A* **387**, 181 (2004). <https://doi.org/10.1016/j.msea.2004.02.083>
27. S. Graff, H. Dierke, S. Forest, H. Neuhäuser, J.L. Strudel, *Philos. Mag.* **88**, 3389 (2008). <https://doi.org/10.1080/14786430802108472>
28. H. Dierke, F. Krawehl, S. Graff, S. Forest, J. Šachl, H. Neuhäuser, *Comput. Mater. Sci.* **39**, 106 (2007). <https://doi.org/10.1016/j.commatsci.2006.03.019>
29. M. Mazière, J. Besson, S. Forest, B. Tanguy, H. Chalons, F. Vogel, *Eur. J. Comput. Mech.* **17**, 761 (2008). <https://doi.org/10.3166/remn.17.761-772>
30. C.P. Ling, P.G. McCormick, *Acta Metall. Mater.* **41**, 3127 (1993). [https://doi.org/10.1016/0956-7151\(93\)90042-Q](https://doi.org/10.1016/0956-7151(93)90042-Q)
31. T. Furuhara, T. Makino, Y. Idei, H. Ishigaki, A. Takada, T. Maki, *Mater. Trans.* **39**, 31 (1998). <https://doi.org/10.2320/matertrans1989.39.31>
32. J. Belotteau, C. Berdin, S. Forest, A. Parrot, C. Prioul, *Mater. Sci. Eng. A* **526**, 156 (2009). <https://doi.org/10.1016/j.msea.2009.07.013>
33. S.Y. Luo, P. Castany, S. Thuillier, *Mater. Sci. Eng. A* **756**, 61 (2019). <https://doi.org/10.1016/j.msea.2019.04.018>
34. N. Guillermin, J. Besson, A. Köster, L. Lacourt, M. Mazière, H. Chalons, S. Forest, *Int. J. Solids Struct.* **264**, 112076 (2023). <https://doi.org/10.1016/j.ijsolstr.2022.112076>
35. S.Y. Luo, P. Castany, S. Thuillier, M. Huot, *Mater. Sci. Eng. A* **733**, 137 (2018). <https://doi.org/10.1016/j.msea.2018.07.022>
36. Y.L. Cai, S.L. Yang, S.H. Fu, D. Zhang, Q.C. Zhang, *J. Mater. Sci. Technol.* **33**, 580 (2017). <https://doi.org/10.1016/j.jmst.2016.05.012>
37. R. Shabadi, S. Kumar, H.J. Roven, E.S. Dwarakadasa, *Mater. Sci. Eng. A* **364**, 140 (2004). <https://doi.org/10.1016/j.msea.2003.08.013>
38. Y.K. Liu, Y.L. Cai, C.G. Tian, G.L. Zhang, G.M. Han, S.H. Fu, C.Y. Cui, Q.C. Zhang, *J. Mater. Sci. Technol.* **49**, 35 (2020). <https://doi.org/10.1016/j.jmst.2020.02.001>
39. T. Tretyakova, M. Tretyakov, *Metals* **13**, 1054 (2023). <https://doi.org/10.3390/met13061054>

**Publisher's Note** Springer Nature remains neutral with regard to jurisdictional claims in published maps and institutional affiliations.

Springer Nature or its licensor (e.g. a society or other partner) holds exclusive rights to this article under a publishing agreement with the author(s) or other rightsholder(s); author self-archiving of the accepted manuscript version of this article is solely governed by the terms of such publishing agreement and applicable law.